CrossMark

Preparation and supercapacitor performance of functionalized graphene aerogel loaded with polyaniline as a freestanding electrode

Chaoke Bulin[1], Huitao Yu[1], Xin Ge[1], Guoxiang Xin[1], Ruiguang Xing[1], Ruihong Li[1], and Bangwen Zhang[1,2,*]

[1] *School of Materials and Metallurgy, Inner Mongolia University of Science and Technology, Baotou 014010, China*
[2] *Instrumental Analysis Center, Inner Mongolia University of Science and Technology, Baotou 014010, China*

ABSTRACT

Graphene aerogel (GA) has wide applications in energy storage, catalysis, and adsorption. However, as a candidate for supercapacitor electrode, it suffers from low specific capacitance. In this paper, we conceived and conducted a two-step strategy to improve the electrochemical properties of GA: First, GA was selective functionalized with *p*-phenylenediamine. Then PANI was grafted onto GA by in situ polymerization. The results suggest that surface functionalization enhances the interface bonding between GA and PANI and charge transfer during electrode redox. As a result, the obtained GA$_p$/PANI composites, applied as the freestanding electrodes for supercapacitor, exhibit high specific capacitance (810 F/g at 1 A/g, 2.4 times of GA), good rate capability, and extraordinary cycling stability (83.2% of retention at 10 A/g after 10,000 cycles, 1.25 times of PANI/GA), indicating its great potential in the construction of high-performance energy-storage systems.

Introduction

With the fast development of sustainable and renewable energy storage technology, supercapacitors have been applied as a novel type of energy storage devices. It is well known for high power density, long cycle life, and high efficiency [1, 2]. For the application of supercapacitors, two categories of electrode materials have been widely exploited and investigated in the last decades, that is, electrical double-layer (EDL) capacitor materials and pseudocapacitive materials [3]. EDL capacitor materials normally employ carbon materials, such as active carbon, carbon nanotubes, and graphene. In particular, three-dimensional (3D) graphene, shaped like hydrogel/aerogel [4], foam/sponges [5] and nano-architectures [6], has recently received increasing attention because of its unique structure and properties, such as self-supported intact skeleton, high porosity, high specific surface area, good electrical conductivity, and perfect flexibility [7–9]. In this respect, 3D graphene is synthesized by electrochemical reduction in graphene oxide (GO) on a gold foil [10] in the literature and results in high areal capacitance

Address correspondence to E-mail: bangwenz@126.com

Springer

(487 mF cm^{-2}) and excellent cycling stability (retention of 93% after 10,000 cycles). Moreover, 3D graphene has exhibited potential in other prospective applications in catalysis [5, 10], adsorption [11], and biological engineering [12].

However, the application of 3D graphene as the candidate of supercapacitor electrodes is limited due to its lower capacitance. The combination of 3D graphene and pseudocapacitive materials is an effective way to tackle this problem. The first choice of pseudocapacitive materials is probably transition metal oxides, such as MnO_2 [13], $Ni(OH)_2$ [14], Co_3O_4 [15], Fe_3O_4 [16]. Though these oxides can provide high pseudocapacitance, they suffer from low flexibility and poor interface interactions with 3D graphene. Recently, other pseudocapacitive materials, especially conducting polymers, such as polyaniline (PANI) [17], polypyrrole [18] and polythiophene, come to the attention of researchers. Meng et al. [19] prepared porous 3D graphene using sacrificial template method and then deposed PANI by a chemical oxidation. The obtained composites have high specific capacitance (385 F/g at 0.5 A/g) and good cycling stability. Liu et al. [20] prepared 3D graphene/PANI based on cellulose fibers using a "dipping and drying" method, which demonstrates higher energy storage (464 F/g). In another research, Xu et al. [21] reported a hybrid electrode of hierarchical PANI-modified carbon nanofiber/graphene oxide with specific capacitance of 450.2 F/g at 10 mV/s. However, few studies on the interface modification between 3D graphene and the conducting polymers were reported. Recent researches have shown it plays an important role in improving the electrochemical performances of conducting polymer/graphene composites [19–26].

In present study, we demonstrate a two-step strategy to improve the electrochemical properties of GA, a typical kind of 3D graphene, as a freestanding supercapacitor electrode: selective functionalization of GA with p-phenylenediamine, grafting of PANI onto GA by in situ oxidation polymerization of aniline. The resultant materials were characterized using FESEM, FTIR, TG, XRD, RS, and XPS techniques. Electrochemical properties of these materials in acidic electrolyte were evaluated through CV, GCD, EIS, and cycling stability tests. Compared with GA and GA/PANI, the functionalized GA/PANI shows superior supercapacitor performance and exhibits good prospects in future energy storage and conversion devices.

Materials and methods

Materials

P-phenylenediamine (p-PDA), aniline (An, AR), sodium nitrite ($NaNO_2$, AR), hydrochloric acid (HCl, AR), and ammonium ammonium sulfate (APS, AR) were purchased from Aladdin Industrial Corporation. Ultrapure water was used throughout the experiments. Graphene oxide was synthesized from powdered flake graphite (300 meshes, Qingdao Meilikun, China) by our improved Hummers method [27].

Synthesis of PANI/GA

As shown in Fig. 1, the preparation process of GA_p/PANI includes three steps, which can be described as follows:

Synthesis of GA

First, 410-mg sodium ascorbate dispersed in 15 mL of H_2O was mixed with 20 mL of 3.5 mg/mL GO and sonicated for 30 min. Subsequently, the suspension was transferred into a Teflon-lined stainless steel autoclave and maintained at 140 °C for 6 h. After being cooled down, the resulting graphene hydrogels were washed repeatedly with distilled water, freeze-dried and finally cylinder-like GA foam was obtained. GA was cut into several discs with a thickness of about 1 mm and weight of about 2 mg.

Functionalization of GA

First, 40 mM p-PDA was dissolved in 40 mL of 1 M HCl aqueous solution under stirring for 10 min, and then 40 mM sodium nitrite was added. After that, GA discs were immersed in the solution under low-velocity stirring, allowing the diazonium reaction in
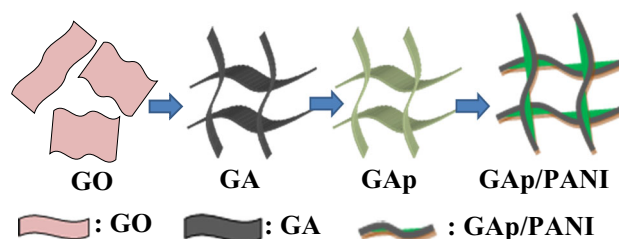

Figure 1 Schematic illustration for preparation processes of GA_p/PANI.

ice bath for 6 h. The products were washed repeatedly with distilled water and freeze-dried. The obtained aniline functionalized GA was named as GA_P.

Synthesis of GA_p/PANI

First, 20 mL of 1 M HCl aqueous solution containing 4 mM aniline was stirred in an ice bath for 10 min, and then GA or GA_P discs were immersed. After 20 mL of 0.2 M APS solution was drop-added into the foregoing solution under stirring for 1 h, the polymerization reaction was kept for x hours ($x = 3$, 6, 9 or 12). The resulting green discs were subsequently raised and freeze-dried, giving the composite samples GA_p/PANI-xh. For comparison, the same procedures were conducted for GA without functionalization, and the resulting products were named as GA/PANI-xh. The mass fraction of PANI in GA/PANI composites was obtained by comparing the mass difference between dried GA and GA/PANI composites.

Characterization

The crystal phases of samples were determined by a powder X-ray diffraction system (XRD, PANalytical, X' Pert PRO, Cu-Ka radiation, $\lambda = 0.15406$ nm). The chemical components and structures were analysed using Fourier transform infrared spectroscopy (FTIR; Bruker, IFS66V), Raman spectroscopy (Raman; Renishaw), and X-ray photoelectron spectroscopy (XPS; Kratos, Axis Supra), and XPS spectra were corrected using the C1s line at 284.6 eV. The morphology was observed by a field-emission scanning electron microscopy (FESEM; JEOL, JSM-6701F), and transmission electron microscope (TEM; JEOL, JEM-2000FX). Thermal gravimetric analyzer (TGA; TA, SDT Q600) was used to test the weight loss of samples with a calefactive rate of 5 °C/min under Ar air flow of 60 mL/min.

Electrochemical tests

Cyclic voltammetry (CV), galvanostatic charge/discharge (GCD), and electrochemical impedance spectroscopy (EIS) tests were conducted to evaluate the electrochemical properties of electrode materials based on a three-electrode cell system: GA_p/PANI(or GA, GA/PANI) as the freestanding working electrode, a Pt plate as counter electrode, and an SCE as reference electrode, and all the electrochemical tests were conducted in 1M H_2SO_4. The CV and EIS data were acquired by an electrochemical workstation (PARSTAT2273, AMETEK), while the GCD data were taken by a Battery Test System (Land 2001, Wuhan Kingnuo, China). Mass specific capacitance C (F/g), energy density W (Wh/kg), and power density P (kW/kg) by the following equations [28]:

$$C = \frac{2I}{m(V_f^2 - V_i^2)} \int_{V_i}^{v_f} V dt \qquad (1)$$

$$E = \frac{I}{3.6m} \int_{V_i}^{v_f} V dt \qquad (2)$$

$$P = 1000 \frac{E}{\Delta t} \qquad (3)$$

where I is the constant discharge current (A), m is the mass of electrode materials (g), Δt is the discharging time(s), V is the potential (V) with initial and final values of V_i and V_f, respectively.

Results and discussion

Characterization

Figure 2 shows the FESEM images of (a) GA, (b) GA_P, (c) GA/PANI-9h and (d) GA_p/PANI-9h, and TEM images of (e) GA/PANI-9h and (f) GA_p/PANI-9h. GA derived from hydrothermal reduction in GO has cylinder-like shape (inset of Fig. 2a) and sponge-like microstructure. Within GA, a mass of macropores interconnect, which allows easy access of liquid media [23], which is key to aniline polymerization and electrolyte diffusion. Compared with its origin GA, GA_P (Fig. 2b) change little in porous morphology, and the difference lies in the N element mapping (bottom inset of Fig. 2b), which arises from the grafted aniline on the surface of GA. After loaded with PANI, the pores become narrow in both GA/PANI-9h (Fig. 2c) and GA_p/PANI-9h (Fig. 2d). Nanometer polyaniline was grown on the surface of graphene uniformly (Fig. 2e, f). But the PANI load of both composites is not high, with a load fraction 10.7 wt% for GA/PANI-9h, 20.9 wt% for GA_p/PANI-9h, respectively. This can be explained by the fact that high-concentration GO colloid (3.5 mg/ml) derived GA has dense narrow pores (Fig. 2b), which prevents the effective diffusion of aniline solution within GA.

Figure 2 FESEM images of **a** GA, **b** GA$_p$, **c** GA/PANI-9h, **d** GA$_p$/PANI-9h, and TEM images of **e** GA/PANI, and **f** GA$_p$/PANI. *Inset* of (**a**) shows the digital image of GA, *insets* of (**b**) show the digital image of GA$_p$ (*top*) and the elemental mapping of GA$_p$ (*bottom*), and *insets* of (**c**), (**d**) and (**f**) shows the corresponding high-magnification image, respectively.
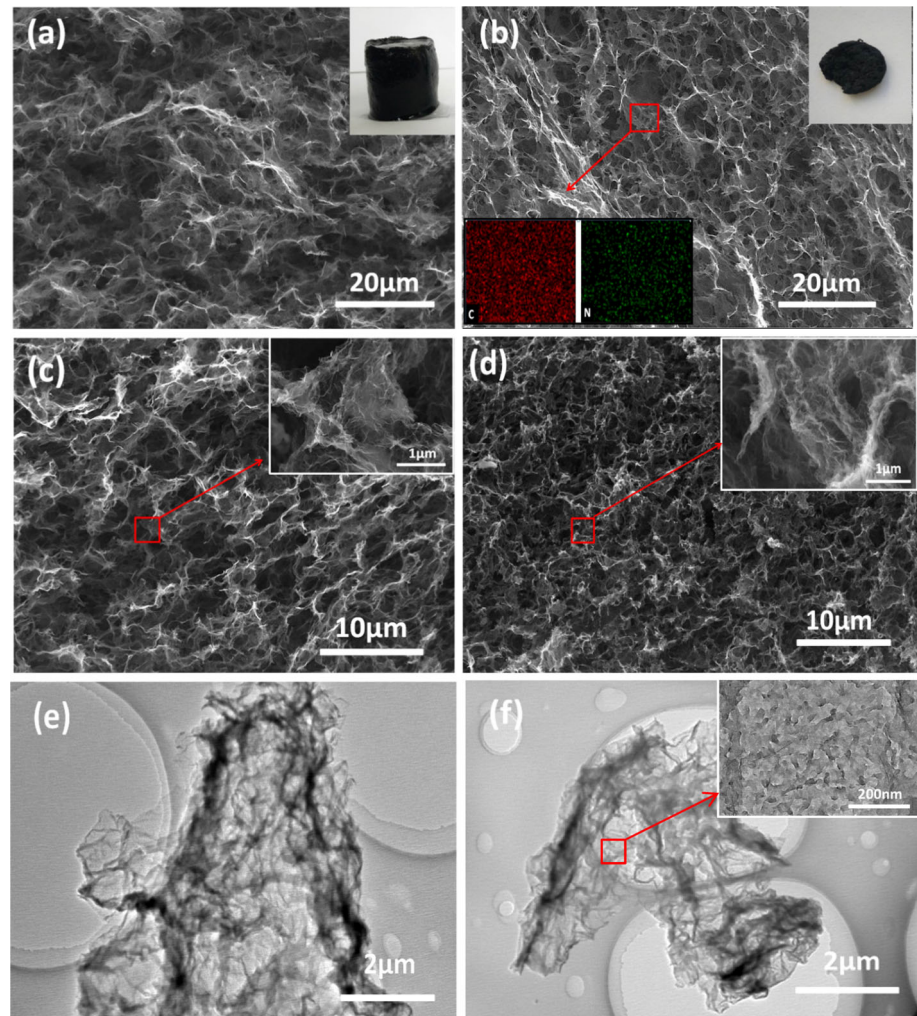

Meantime, the polymerization reaction would be limited due to the dilute monomer (0.1 mM/ml). However, the case can be improved by functionalization of graphene, which can enhance the surface wettability and reaction activity of GA and afford it higher load of PANI.

Figure 3a illustrates the FTIR spectra of GO, GA, GA$_p$, PANI, and GA$_p$/PANI-9h. The spectrum of GO showed strong absorption at 3400, 1729, 1400, and 1060 cm^{-1} due to –OH, –C=O vibration in COOH and C–O vibration in C–OH/C–O–C [27]. A sharp band around 1625 cm^{-1} might be from the intramolecular H$_2$O. Due to the reduction, most peaks in GA become weak or disappear except for –COOH group, which remains in the edge of graphene planes. In the spectrum of GA$_p$, new bands at 840 and 1147 cm^{-1} are assigned to the vibration of N–H and C–N, suggesting that –NH$_2$ was grafted on the surfaces of GA$_p$. The resultant GA$_p$/PANI-9h exhibits similar characteristic peaks as compared to the pure PANI. For GA$_p$/PANI-9h, the peaks at 1299, 1246, 1145, and 818 cm^{-1} are attributed to the C–N stretching vibration of the benzene ring, stretching vibration of the C–N in the polaron structure of PANI, stretching of C=N and out-of-plane bending vibration of C–H in benzene ring, respectively [29]. Compared with GA$_p$, the main bands centered at 3440, 1566, and 1485 cm^{-1} can be ascribed to N–H stretching, C–C stretching vibration of the quinoid ring and the C–C benzenoid ring in PANI, indicating the presence of PANI [20]. Figure 3b shows the TGA of GO, GA, GA$_p$, and GA$_p$/PANI-9h. The initial weight loss occurs at about 150 °C, which is correlated with the pyrolysis of the bound water. This is followed by a significant weight loss between 200 and 300 °C, indicating the pyrolysis of the oxidized groups of GO and GA, grafted molecule of GA$_p$ and

Figure 3 a FTIR of GO, GA, GA$_p$, PANI, and GA$_p$/PANI-9h, **b** TGA of GO, GA, GA$_p$ and GA$_p$/PANI-9h.
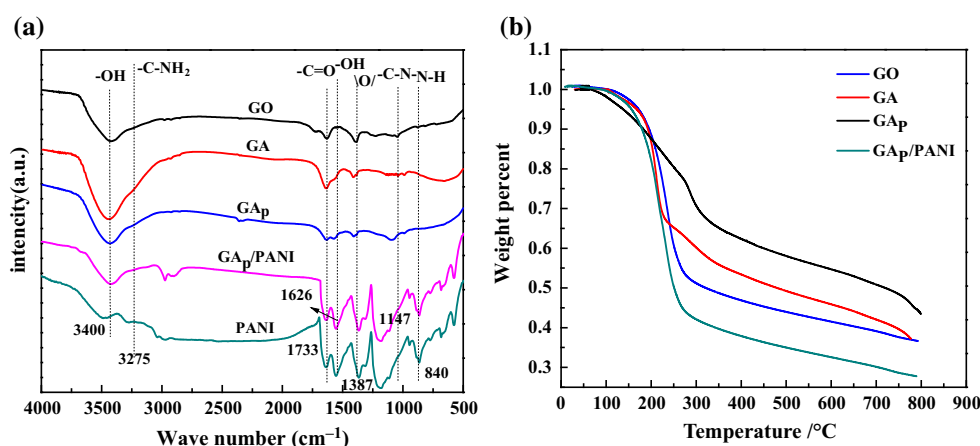
PANI bonded on GA [27]. The order of thermal stability is GA$_p$/PANI-9h < GO < GA < GA$_p$.

Figure S1 gives the XRD patterns of GO, GA$_p$, GA$_p$/PANI-9h. GO has a characteristic diffraction peak at $2\theta = 10.31°$, corresponding to the (110) interplanar spacing of 7.3 Å [27, 30], and GA$_p$ is characterized by the peak at 23.2° (d$_{(002)}$ = 3.7 Å), which indicates the formation of a poorly ordered graphite-like material (d$_{(002)}$ = 3.4 Å for graphite). For GA$_p$/PANI-9h, the crystalline peaks at about 20° and 25° can be assigned to (020) and (002) reflections of PANI in its polyaniline salt form, while two broad diffraction peaks around 25° present the (002) facets of the hexagonal graphitic results from GA$_p$ [30]. Figure S2 shows the Raman spectra of GO and GA$_p$, where D band at 1360 cm^{-1} and G band at 1574 cm^{-1} can be attributed to the conversion of a sp^2-hybridized carbon to a sp^3-hybridized carbon, and the in-plane bond-stretching motion of the pairs of C sp^2 atoms, respectively [27]. For GO and GA$_p$, the intensity ratio D band to G band I_D/I_G = 0.94, 1.12, respectively. The increased I_D/I_G of GA relative to GO indicates the realization of deoxygenation in chemically reduced graphene.

XPS was employed to determine the element and bond composition of GO, GA, GA$_p$, and GA$_p$/PANI-9h. The survey spectra (Fig. 4a) confirm that the main elements C (C1s) and O (O1s) resulting from all samples, and N element (N1s) only from GA$_p$ and GA$_p$/PANI-9h samples [31]. As is expected, GO has higher O1s peak than GA, and GA$_p$/PANI has higher N1s peak than GA$_p$. In C1s spectrum of GO (top of Fig. 4b), four types of covalently bonded carbon can be resolved as sp^2 carbon (C–C/C=C, 284.6 eV), epoxy/hydroxyl groups (C–O, 286.6 eV), carbonyl

groups (C=O, 287.8 eV), and carboxyl groups (O–C=O, 289.5 eV), respectively [27, 32]. After reduction in GO, the C–O bonds are greatly reduced, so C1s spectra of GA, GA$_p$, and GA$_p$/PANI-9h(middle and bottom of Fig. 4b) shift to lower binding energy. In C1s spectra of GA$_p$ and GA$_p$/PANI-9h, new C–N bond can be isolated at 286.8 eV among the deconvoluted peaks, indicating the successful bonding of N element in GA$_p$ and GA$_p$/PANI-9h. In contrast, C–N bond could not be isolated from the C1s spectrum of GA. The N1s spectra (Fig. 4c) of GA$_p$ and GA$_P$/PANI-9h can be resolved into four peaks located at 398.8, 399.6, 400.3, and 401.7 eV, corresponding to benzenoid amine (=N–), quinoid amine (–NH–), nitrogen cationic radical (NH$^+$), and amino positive ion (NH$_2^+$=) [33], respectively. Due to the presence of PANI, GA$_P$/PANI has much higher NH$_2^+$ = peak than GA$_p$.

To interpret the formation process of GA$_p$/PANI, we propose a mechanism description, as shown in Fig. 5. First, hydrothermal reduction in GO constructs the 3D framework of GA, drove by the interactions such as hydrophobic–hydrophilic and π–π stacking interactions [10], and some carboxyl remain in the edge of basal plane of graphene; second, the p-PDA functionalization of GA introduces covalent aniline in basal plane of graphene through diazonium reaction and leads to GA$_p$; third, beginning with those active cites, major functionalized aniline and few carboxyl, PANI molecule produced by oxidization polymerization of aniline monomers heterogeneously nucleate and grow, and finally form the PANI/GA$_p$ composites. Due to the improvement in surface wettability and reaction activity, GA$_p$ can absorb and load higher amount of PANI relative to

Figure 4 XPS spectra of samples **a** survey, **b** C1s and **c** N1s.
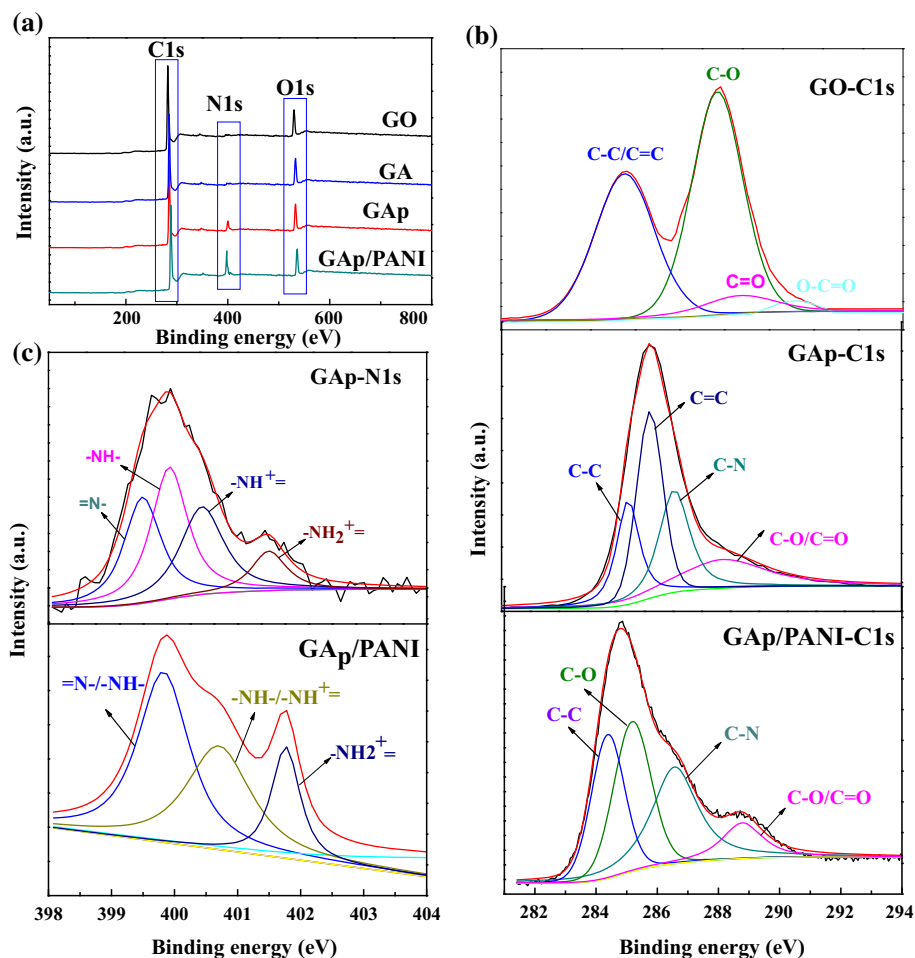
GA by in situ polymerization, affording it large pseudocapacitance as a supercapacitor electrode.

Electrochemical properties

The CV and GCD curves of GA, GA_p, GA/PANI-8h, and GA_p/PANI-8h were determined to evaluate the electrochemical properties. Figure 6a shows GA and GA_p share similar and smooth CV loops, which indicates the EDL capacitance is most contributive, while the functionalization of GA has not significant effect on the capacitance. When GA and GA_p are coupled with PANI, the CV curves observe a new couple of redox peaks from the pseudocapacitive PANI [34], and GA_p/PANI-8h has a much larger loop area or specific capacitance than GA/PANI-8h, which can be attributed to the enhanced interface bonding and PANI load within GA_p. Figure 6b illustrates the CV curves of GA_p/PANI obtained for different reaction time (x = 3, 6, 9, 12 h). It shows that with the increase in reaction time, the loop area first

increases and finally decreases, and reaches the maximum value at x = 9 h, which corresponds to the largest specific capacitance. For the GA_p/PANI-9h, we further investigated the charge/discharge performance (Fig. 6c). The GCD curves appear nonlinear and symmetrical. As EDL capacitance often behaves linearly during charge/discharge, the nonlinearity indicates that there exists pseudocapacitance in electrode materials. Furthermore, the symmetry of the GCD curve implies that electrode materials work rather stably, owing to the supporting of 3D GA. As the current density increases, the charge/discharge time decreases. With a current density of 5 A/g, the charge/discharge finished fast within 80 s. With a current density of 0.5 A/g, a specific capacitance of 905 F/g is obtained. This value is superior over the reported results [35–37]. To further evaluate and compare the rate performance, we plot the specific capacitance versus current density in Fig. 6d for GA, GA/PANI-9h and GA_p/PANI-9h. Clearly, the specific capacitance stored by GA_p/PANI-9h
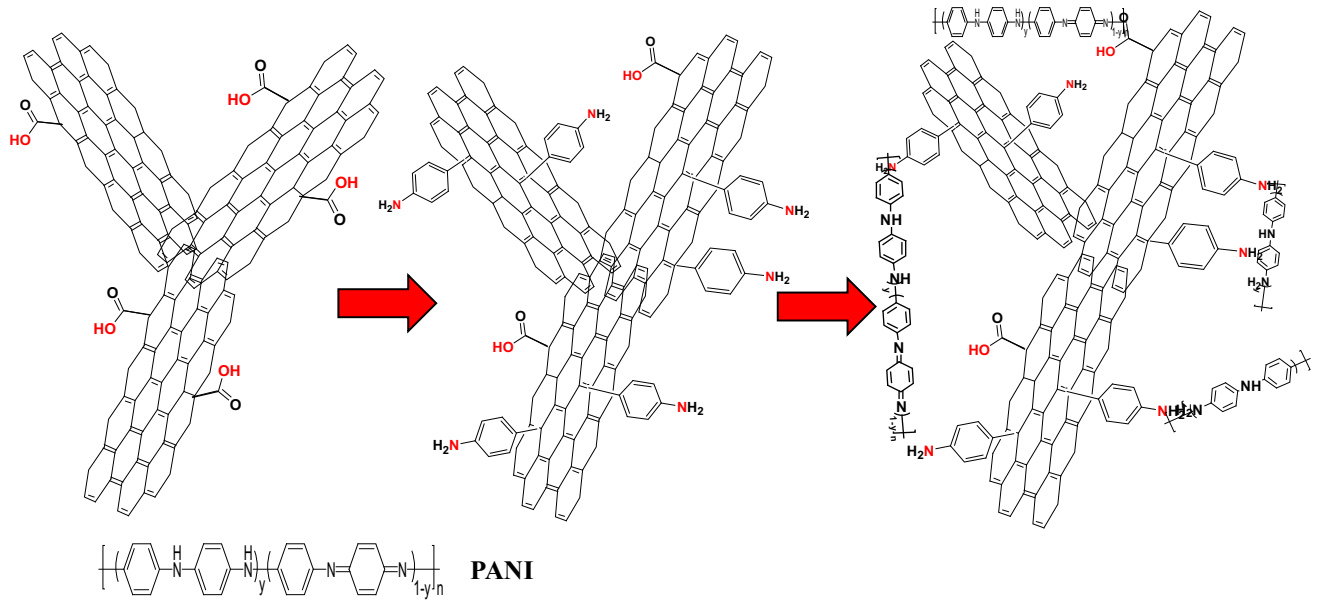
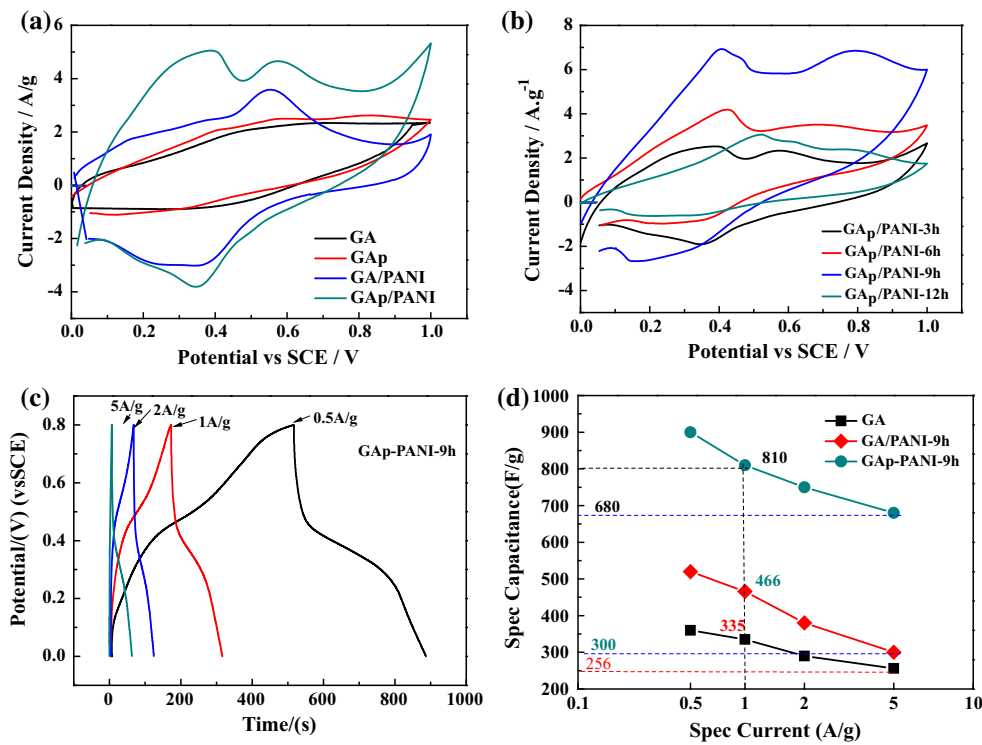**Figure 5** Mechanism description of the synthesis of GA$_p$/PANI.

Figure 6 Electrochemical tests **a** CV *curves* of GA, GA$_P$, GA/PANI-8h, and GA$_P$/PANI-8h at 5 mV s^{-1}, **b** CV *curves* of GA$_p$/PANI-x ($x = 3, 6, 9, 12$ h) at 5 mV s^{-1}, **c** GCD *curves* of GA$_p$/PANI-9h at current density of 0.5, 1, 2, 5 A/g, **d** specific capacitance of GA/PANI and GA$_p$/PANI.

dominates over the other two. For example, this value at 1 A/g is 810 F/g for GA$_P$/PANI-9h, and 335 F/g for GA and 466 F/g for GA/PANI-9h. Second, the capacitance declines slowly cross a wide range of current density, suggesting that the materials are of good rate capability. For GA$_P$/PANI-9h, the capacitance only loses 25% of its initial value when the current density increases from 0.5 to 5 A/g. So it is

Figure 7 EIS of GA, GA$_P$, GA/PANI-9h and GA$_P$/PANI-9h. **a** Nyquist plot and **b** imaginary capacitance versus frequency.
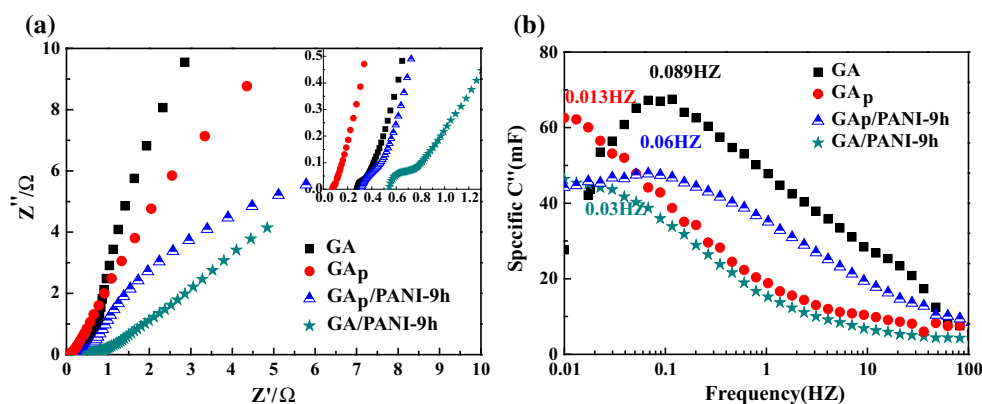
necessary for the functionalization of GA and coupling of PANI in GA as dual strategies to improve the capacitance performance of GA.

EIS is an effective tool to judge the charge transport phenomena of electrode materials [38]. Nyquist (Z'–Z'') plot of GA, GA$_P$, GA/PANI-9h, and GA$_P$/PANI-9h was measured from 10 kHz to 0.1 Hz. Theoretically, the Z'–Z'' curves have two segments, a low frequency region (right) and a high frequency region (left), and the latter often emerges as a semicircle. Moreover, the semicircle is characterized by a starting point standing for the equivalent series resistances R_i and a diameter for the electrode/electrolyte interface charge transfer resistance R_{CT} [37, 39]. Figure 7a shows as supported by the conducting GA, R_i of GA, GA$_P$, and GA$_P$/PANI-9h is low, but that of GA/PANI is maximum (0.55 Ω). Furthermore, the corresponding R_{CT} is also small, and GA/PANI still has the maximum value, indicating weak interface bonding resists the charge transfer. Figure 7b plots the imaginary capacitance as a function of frequency. From the location of peaks, one can determine the

characteristic frequency f_0 and time constant $\tau = 1/2\pi f_0$. It shows $\tau = 1.79$, 12.2, 16 and 2.65 s for GA, GA$_P$, GA/PANI-9h, and GA$_P$/PANI-9h, respectively, so GA$_P$/PANI-9h has lower value of τ than GA/PANI-9h, further suggesting surface functionalization can improve the kinetics of charge transfer cross the electrodes.

Figure 8a evaluates the cycling performance of capacitance for GA, GA/PANI-9h and GA$_P$/PANI-9h, by GCD at a current density of 10 A/g for 10,000 cycles [27, 40]. The retention of capacitance for GA, GA/PANI-9h, and GA$_P$/PANI-9h is 98.18, 67, and 83.2%, respectively, that is, the cycling stability of GA/PANI-9h is far less than that of the other two. This might be because of the partial detachment of PANI from GA substrate during the long-term cycling [41], due to the absence of strong interface bonding between PANI and GA. In contrast, thanks to the strong bonding between functionalized GA and PANI, GA$_P$/PANI exhibits high cycling stability. Figure 8b presents Ragone plot of the three samples. It shows after loaded with PANI, the energy density
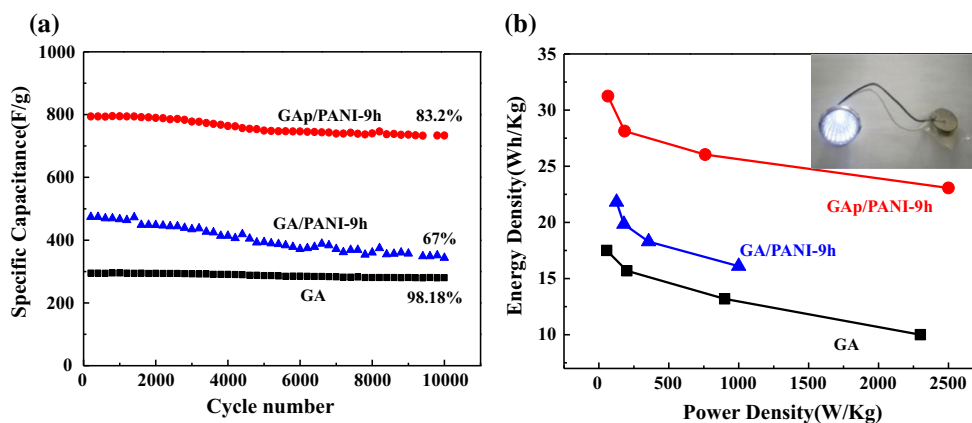

Figure 8 **a** Cycling performance of capacitance and **b** Ragone plot of GA, GA/PANI-9h and GA$_p$/PANI-9h.

of GA noticeably increases, and GA$_p$/PANI-9h possesses both high energy density and high power density. Further, we assembled a symmetric supercapacitor based on GAp/PANI-9h (inset of Fig. 8b), which can lighten a LED lamp for 5 min. The tested results (Fig. S3, Supplementary) show it has a specific capacitance of 211.2 F/g, about 25% of that value of three-electrode system, and a long circle life, consistent with the three-electrode system.

Conclusions

In summary, in present research we demonstrated a new routine to prepare high-performance GA/PANI composites as the freestanding electrodes for supercapacitor. The routine includes two key steps: (1) selective functionalization of GA with p-phenylenediamine via the diazonium reaction, (2) the grafting of the pseudocapacitive PANI onto GA by in situ oxidation polymerization. The obtained materials were characterized using various instrumental methods, such as FESEM, TEM, FTIR, TG, RS, and XPS, and their formation mechanisms and electrochemical properties were investigated in details. The results suggest that owing to the application of surface functionalization, the interface bonding between GA and PANI, the load of PANI and the electrode/electrolyte interface charge transfer during electrode redox were enhanced. Therefore, as compared to GA and nonfunctionalized GA/PANI, the functionalized GA/PANI composites exhibit superior supercapacitor performance. Our work not only highlights the importance of interface modification in composite design, but also provides a proper routine for the development of high-performance supercapacitors.

Acknowledgements

Electronic supplementary material: The online version of this article (doi:10.1007/s10853-017-0823-1) contains supplementary material, which is available to authorized users.

References

[1] Zhao YH, Zhang YF, Wu ZK, Bai SL (2016) Synergic enhancement of thermal properties of polymer composites by graphene foam and carbon black. Compos B Eng 84:52–58

[2] Long JW, Bélanger D, Brousse T, Sugimoto W, Sassin MB, Crosnier O (2011) Asymmetric electrochemical capacitors-stretching the limits of aqueous electrolytes. MRS Bull 36(07):513–522

[3] Zhang Z, Xiao F, Guo Y, Wang S, Liu Y (2013) One-pot self-assembled three-dimensional TiO$_2$-graphene hydrogel with improved adsorption capacities and photocatalytic and electrochemical activities. ACS Appl Mater Interfaces 5(6):2227–2233

[4] Chi K, Zhang Z, Xi J, Huang Y, Xiao F, Wang S, Liu Y (2014) Freestanding graphene paper supported three-dimensional porous graphene–polyaniline nanocomposite synthesized by inkjet printing and in flexible all-solid-state supercapacitor. ACS Appl Mater Interfaces 6(18):16312–16319

[5] Chen Z, Ren W, Gao L, Liu B, Pei S, Cheng HM (2011) Three-dimensional flexible and conductive interconnected graphene networks grown by chemical vapour deposition. Nat Mater 10(6):424–428

[6] Chung DDL (2016) A review of exfoliated graphite. J Mater Sci 51(1):554–568. doi:10.1007/s10853-015-9284-6

[7] Choi BG, Yang M, Hong WH, Choi JW, Huh YS (2012) 3D macroporous graphene frameworks for supercapacitors with high energy and power densities. ACS Nano 6(5):4020–4028

[8] Wang ZL, Xu D, Wang HG, Wu Z, Zhang XB (2013) In situ fabrication of porous graphene electrodes for high-performance energy storage. ACS Nano 7(3):2422–2430

[9] Zhang R, Cao Y, Li P, Zang X, Sun P, Wang K, Zhong M, Wei J, Wu D, Kang F, Zhu H (2014) Three-dimensional porous graphene sponges assembled with the combination of surfactant and freeze-drying. Nano Res 7(10):1477–1487

[10] He S, Chen W (2015) 3D graphene nanomaterials for binder-free supercapacitors: scientific design for enhanced performance. Nanoscale 7(16):6957–6990

[11] Li W, Gao S, Wu L, Qiu S, Guo Y, Geng X, Chen M, Liao S, Zhu C, Gong Y, Xu J, Wei X, Sun M, Liu L, Long M (2013) High-density three-dimension graphene macroscopic objects for high-capacity removal of heavy metal ions. Sci Rep 3:2125

[12] Wang W, Guo S, Ruiz I, Ozkan M, Ozkan CS (2013) Three dimensional graphene-CNTs foam architectures for electrochemical capacitors. ECS Trans 50(43):37–44

[13] Zhang Z, Xiao F, Qian L, Xiao J, Wang S, Liu Y (2014) Facile synthesis of 3D MnO2–graphene and carbon nanotube-graphene composite networks for high-performance, flexible, all-solid-state asymmetric supercapacitors. Adv Energy Mater 4(10):867–872

[14] Fujisawa K, Cruz-Silva R, Yang KS, Kim YA, Hayashi T, Endo M, Terrones M, Dresselhaus MS (2014) Importance of open, heteroatom-decorated edges in chemically doped-graphene for supercapacitor applications. J Mater Chem A 2(25):9532–9540

[15] Rakhi RB, Chen W, Cha D, Alshareef HN (2012) Substrate dependent self-organization of mesoporous cobalt oxide nanowires with remarkable pseudocapacitance. Nano Lett 12(5):2559–2567

[16] Wang H, Xu Z, Yi H, Wei H, Guo Z, Wang X (2014) One-step preparation of single-crystalline Fe_2O_3 particles/graphene composite hydrogels as high performance anode materials for supercapacitors. Nano Energy 7:86–96

[17] Zhang Z, Chi K, Xiao F, Wang S (2015) Advanced solid-state asymmetric supercapacitors based on 3d graphene/MnO_2 and graphene/polypyrrole hybrid architectures. J Mater Chem A 3(24):12828–12835

[18] Wang G, Zhang L, Zhang J (2012) A review of electrode materials for electrochemical supercapacitors. Chem Soc Rev 2:797–828

[19] Meng Y, Wang K, Zhang Y, Wei Z (2013) Hierarchical porous graphene/polyaniline composite film with superior rate performance for flexible supercapacitors. Adv Mater 25(48):6985–6990

[20] Liu L, Niu Z, Zhang L, Zhou W, Chen X, Xie S (2014) Nanostructured graphene composite papers for highly flexible and foldable supercapacitors. Adv Mater 26(28):4855–4862

[21] Xu D, Xu Q, Wang K, Chen J, Chen Z (2013) Fabrication of free-standing hierarchical carbon nanofiber/graphene oxide/polyaniline films for supercapacitors. ACS Appl Mater Interfaces 6(1):200–209

[22] Wang W, Guo S, Penchev M, Ruiz I, Bozhilov KN, Yan D, Ozkan M, Ozkan CS (2013) Three dimensional few layer graphene and carbon nanotube foam architectures for high fidelity supercapacitors. Nano Energy 2(2):294–303

[23] Fan H, Zhao N, Wang H, Xu J, Pan F (2014) 3D conductive network-based free-standing PANI-RGO-MWNTs hybrid film for high-performance flexible supercapacitor. J Mater Chem A 2(31):12340–12347

[24] Chen W, He Y, Li X, Zhou J, Zhang Z, Zhao C, Gong C, Li S, Pan X, Xie E (2013) Facilitated charge transport in ternary interconnected electrodes for flexible supercapacitors with excellent power characteristics. Nanoscale 5(23):11733–11741

[25] Liang M, Zhi L (2009) Graphene-based electrode materials for rechargeable lithium batteries. J Mater Chem 19(33):5871–5878

[26] Meng C, Liu C, Fan S (2009) Flexible carbon nanotube/polyaniline paper-like films and their enhanced electrochemical properties. Electrochem Commun 11(1):186–189

[27] Yu H, Zhang B, Bulin C, Li R, Xing R (2016) High-efficient synthesis of graphene oxide based on improved hummers method. Sci Rep 6:36143

[28] Mai LQ, Minhas-Khan A, Tian X, Hercule KM, Zhao YL, Lin X, Xu X (2013) Synergistic interaction between redox-active electrolyte and binder-free functionalized carbon for ultrahigh supercapacitor performance. Nat Commun 4:2923

[29] Salvatierra RV, Cava CE, Roman LS, Zarbin AJ (2013) ITO-free and flexible organic photovoltaic device based on high transparent and conductive polyaniline/carbon nanotube thin films. Adv Funct Mater 23(12):1490–1499

[30] Domingues SH, Salvatierra RV, Oliveira MM, Zarbin AJ (2011) Transparent and conductive thin films of graphene/polyaniline nanocomposites prepared through interfacial polymerization. Chem Commun 47(9):2592–2594

[31] Salvatierra RV, Oliveira MM, Zarbin AJ (2010) One-pot synthesis and processing of transparent, conducting, and freestanding carbon nanotubes/polyaniline composite films. Chem Mater 22(18):5222–5234

[32] McAllister MJ, Li JL, Adamson DH, Schniepp HC, Abdala AA, Liu J, Herrera-Alonso MiliusLD, Car R, Prud'homme RK, Aksay IA (2007) Single sheet functionalized graphene by oxidation and thermal expansion of graphite. Chem Mater 19(18):4396–4404

[33] Wang S, Ma L, Gan M, Fu S, Dai W, Zhou T, Sun X, Wang H, Wang H (2015) Free-standing 3D graphene/polyaniline composite film electrodes for high-performance supercapacitors. J Power Sources 299:347–355

[34] Lee T, Yun T, Park B, Sharma B, Song HK, Kim BS (2012) Hybrid multilayer thin film supercapacitor of graphene nanosheets with polyaniline: importance of establishing intimate electronic contact through nanoscale blending. J Mater Chem 22(39):21092–21099

[35] Hyder MN, Lee SW, Cebeci FÇ, Schmidt DJ, Shao-Horn Y, Hammond PT (2011) Layer-by-layer assembled polyaniline nanofiber/multiwall carbon nanotube thin film electrodes for high-power and high-energy storage applications. ACS Nano 5(11):8552–8561

[36] Yu P, Zhao X, Huang Z, Li Y, Zhang Q (2014) Free-standing three-dimensional graphene and polyaniline nanowire arrays hybrid foams for high-performance flexible and lightweight supercapacitors. J Mater Chem A 2(35):14413–14420

[37] Khoh WH, Hong JD (2013) Layer-by-layer self-assembly of ultrathin multilayer films composed of magnetite/reduced graphene oxide bilayers for supercapacitor application. Colloids Surf A 436:104–112

[38] Augustyn V, Simon P, Dunn B (2014) Pseudocapacitive oxide materials for high-rate electrochemical energy storage. Energy Environ Sci 7(5):1597–1614

[39] Kulkarni SB, Patil UM, Shackery I, Sohn JS, Lee S, Park B, Jun S (2014) High-performance supercapacitor electrode based on a polyaniline nanofibers/3D graphene framework as an efficient charge transporter. J Mater Chem A 2(14):4989–4998

[40] Sarker AK, Hong JD (2012) Layer-by-layer self-assembled multilayer films composed of graphene/polyaniline bilayers: high-energy electrode materials for supercapacitors. Langmuir 28(34):12637–12646

[41] Zhi M, Xiang C, Li J, Li M, Wu N (2013) Nanostructured carbon–metal oxide composite electrodes for supercapacitors: a review. Nanoscale 5(1):72–88